

Article

Scale Effects on Quasi-Steady Solid Rocket Internal Ballistic Behaviour

David R. Greatrix

Department of Aerospace Engineering, Ryerson University, 350 Victoria Street, Toronto, Ontario, M5B2K3, Canada; E-Mail: greatrix@ryerson.ca; Tel.: +1-416-979-5000 ext. 6432; Fax: +1-416-979-5056.

Received: 23 October 2010; in revised form: 4 November 2010 / Accepted: 11 November 2010 / Published: 15 November 2010

Abstract: The ability to predict with some accuracy a given solid rocket motor's performance before undertaking one or several costly experimental test firings is important. On the numerical prediction side, as various component models evolve, their incorporation into an overall internal ballistics simulation program allows for new motor firing simulations to take place, which in turn allows for updated comparisons to experimental firing data. In the present investigation, utilizing an updated simulation program, the focus is on quasi-steady performance analysis and scale effects (influence of motor size). The predicted effects of negative/positive erosive burning and propellant/casing deflection, as tied to motor size, on a reference cylindrical-grain motor's internal ballistics, are included in this evaluation. Propellant deflection has only a minor influence on the reference motor's internal ballistics, regardless of motor size. Erosive burning, on the other hand, is distinctly affected by motor scale.

Keywords: solid rocket motor internal ballistics; scale effects; quasi-steady operation

Nomenclature

A = local core cross-sectional area (m^2)

a_t = longitudinal (or lateral) acceleration (m/s^2)

a_n = normal acceleration (m/s^2)

C_p = gas specific heat (J/kg-K)

D = drag force of gas on particle (N)

d = local core hydraulic diameter (m)

$d_{p,i}$ = initial grain port diameter (m)

- E = local total specific energy of gas in core (J/kg)
 E_p = local total specific energy of particles in flow (J/kg)
 f = Darcy-Weisbach friction factor
 f_{lim} = limit friction factor for negative erosive burning
 ΔH_s = net surface heat of reaction (J/kg)
 h = convective heat transfer coefficient (W/m²-K)
 K = lateral/longitudinal acceleration vector correction coefficient
 K_δ = shear layer coefficient (m⁻¹)
 ℓ_p = propellant grain length (m)
 m_p = mass of particle (kg)
 p = local gas static pressure (Pa)
 Q = heat transfer from gas to particle (W)
 r_b = overall propellant burning rate (m/s)
 r_o = base burning rate (m/s)
 T_f = flame temperature, gas phase (K)
 T_i = initial temperature, solid phase (K)
 T_s = burning surface temperature (K)
 t = time (s)
 u = core axial gas velocity (m/s)
 u_p = axial particle velocity (m/s)
 v_f = nominal flamefront velocity (m/s)
 x = axial distance from head end (m)
 α_p = particle loading mass fraction
 ε = propellant surface roughness (m)
 ρ = gas density (kg/m³)
 ρ_p = particle density in flow (kg/m³)
 ρ_s = solid propellant density (kg/m³)
 ϕ = nominal acceleration vector orientation angle (deg)
 ϕ_d = displacement-correction orientation angle (deg)

1. Introduction

With respect to the internal ballistics of solid-propellant rocket motors (SRMs), ideally one should be able to understand and quantitatively predict the behaviour of a given motor, prior to undertaking an experimental test firing. A comprehensive numerical model for simulation of the respective flow and combustion conditions is essential. An effective model combines the effects of the flow, the combustion process, and where applicable, the structural behaviour of the surrounding propellant/casing structure. With respect to internal ballistic analyses, one typically separates these into two main categories: (1) quasi-steady analysis, and (2) unsteady analysis. In the first category, local parameters for the most part are changing relatively slowly with time, such that the nominal main firing profile (chamber pressure, thrust, *etc.*, as a function of time) can (usually) be readily computed (with the exclusion of the unsteady initial ignition transient and final chamber-emptying tailoff phases

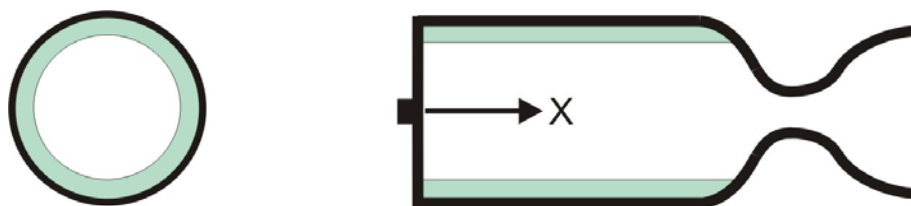
that bound the main profile [1]). With regards to the second category, certain local parameters are changing relatively rapidly with time, for example during the abovementioned ignition/filling process, or when a pressure wave disturbance has been introduced into the core flow, where one tends to focus on short periods of time within the motor firing simulation (in part due to computational limitations on simulation turnaround times). On the numerical prediction side, as various component models evolve, their incorporation into an overall internal ballistics simulation program allows for new motor firing simulations to take place, which in turn allows for updated comparisons to available experimental firing data, and a better understanding of the influence of various factors.

In the present investigation, the focus will be on quasi-steady analysis [2], with consideration of the predicted effects of negative/positive erosive burning and propellant/casing deflection as tied to the motor's size (moving from smaller to larger motor lengths and port diameters). While there is some discussion in the present paper of the treatment of inert particles for a more general two-phase quasi-steady flow solution, for brevity, example results presented later in the paper will be limited to the simpler single-phase case (gas only). Similarly, while the effect of acceleration (due to spinning of the motor) on the burning process is outlined to some degree to provide some general background to the reader, example results will be restricted to non-spinning cases. Example results are presented in this paper in order to provide the reader with some background on the sensitivities of various pertinent parameters, with the present study focusing on a reference cylindrical-grain SRM that is scaled up in size.

2. Numerical Model

The fundamental, and simplest, configuration of an SRM for theoretical studies is the standard radially burning cylindrical-grain design illustrated by Figure 1. Under normal (nominal) quasi-equilibrium operating conditions, the internal gas flow (or gas-particle flow, if two-phase) moves smoothly from the burning propellant surface into the axial core (port), and continuing along the propellant grain's port, ultimately through and beyond the exhaust nozzle.

Figure 1. Schematic diagram of cylindrical-grain SRM, showing reference x -direction.



The equations of motion describing the steady-state core flow within the SRM must be solved in conjunction with the local surface regression rate r_b of the solid propellant, and the surrounding structure's current geometric deformation. As pertains to the present study of a motor having a larger length-to-diameter ratio, the quasi-one-dimensional quasi-steady hydrodynamic conservation equations for the axial gas flow are given below (from [2]):

$$\frac{d(\rho u)}{dx} = -\frac{1}{A} \frac{dA}{dx} \rho u + (1 - \alpha_p) \rho_s \frac{4r_b}{d} - \left(\frac{4r_b}{d}\right) \rho \quad (1)$$

$$\frac{d}{dx}(\rho u^2 + p) = -\frac{1}{A} \frac{dA}{dx} \rho u^2 - \left(\frac{4r_b}{d}\right) \rho u - \rho a_\ell - \frac{\rho_p}{m_p} D \quad (2)$$

$$\begin{aligned} \frac{d}{dx}(\rho u E + up) &= -\frac{1}{A} \frac{dA}{dx} (\rho u E + up) - \left(\frac{4r_b}{d}\right) \rho E \\ &+ (1 - \alpha_p) \rho_s \frac{4r_b}{d} \left(C_p T_f + \frac{v_f^2}{2}\right) - \rho u a_\ell - \frac{\rho_p}{m_p} (u_p D + Q) \end{aligned} \quad (3)$$

Here, the total specific energy of the gas is defined for an ideal gas as $E = p/[(\gamma-1)\rho] + u^2/2$. The corresponding quasi-steady equations of motion for a monodisperse inert (non-burning) particle phase within the axial flow may be found as follows (from [2]):

$$\frac{d(\rho_p u_p)}{dx} = -\frac{1}{A} \frac{dA}{dx} \rho_p u_p + \alpha_p \rho_s \frac{4r_b}{d} - \left(\frac{4r_b}{d}\right) \rho_p \quad (4)$$

$$\frac{d(\rho_p u_p^2)}{dx} = -\frac{1}{A} \frac{dA}{dx} \rho_p u_p^2 - \left(\frac{4r_b}{d}\right) \rho_p u_p - \rho_p a_\ell + \frac{\rho_p}{m_p} D \quad (5)$$

$$\begin{aligned} \frac{d(\rho_p u_p E_p)}{dx} &= -\frac{1}{A} \frac{dA}{dx} (\rho_p u_p E_p) - \left(\frac{4r_b}{d}\right) \rho_p E_p \\ &+ \alpha_p \rho_s \frac{4r_b}{d} \left(C_m T_f + \frac{v_f^2}{2}\right) - \rho_p u_p a_\ell + \frac{\rho_p}{m_p} (u_p D + Q) \end{aligned} \quad (6)$$

Here, the total specific energy of a local grouping of particles is given by $E_p = C_m T_p + u_p^2/2$, where T_p is the mean temperature of that group. As outlined in [2,3], the viscous interaction between the gas and particle phases is represented by the drag force D , and the heat transfer from the core flow to the particles is defined by Q . Here, longitudinal acceleration a_ℓ appears in the gas and particle momentum and energy equations as a body force contribution within a fixed Eulerian reference (fixing of $x = 0$ to motor head end, x positive moving right on structure; acceleration of local surrounding structure rightward is designated positive a_ℓ), and may vary both spatially along the length of the motor and with time. The effects of such factors as turbulence can be included through one or more additional equations that employ the information from the bulk flow properties arising from the solution of the above one-dimensional equations of motion.

The ideal equation of state for a gas is commonly employed in SRM simulations, with flow properties closer to the thermochemically frozen value than the equilibrium value, for calculations in the motor chamber. The above ideal-gas assumption precludes the effects of chemical reactivity within and along the central core flow of the chamber, as a drawback of this simplification. Moving downstream, one must acknowledge that the flow properties would tend to get closer to thermochemical equilibrium when passing through, and then beyond, the exhaust nozzle.

The principal ordinary differential equations themselves can be solved via a suitable finite-difference approach [2]. One makes an appropriate choice for spatial increment in the axial direction, Δx , for calculations along the grain and nozzle for a given point in the firing, and time increment, Δt , to progress to the next point in the firing, so that one adequately captures the quasi-steady characteristics of the given simulated firing segment. In practice, both Δx and Δt can be quite large (there are no hard

numerical stability limits in this quasi-steady solution case, unlike fully unsteady flows that are governed by the Courant-Friedrichs-Lewy [CFL] criterion) and still produce a reasonably accurate quasi-steady firing profile. However, it is best to make them small enough so that changes in various pertinent parameters are on the order of a few percent, in moving from one increment to the next, in space or time.

Structural deformation can potentially play a role in quasi-steady SRM internal ballistic behaviour, the principal effect of interest being the increase in local internal port cross-sectional area under pressure loading. The level of sophistication required for modeling the motor structure (propellant, casing, nozzle) and applicable boundary conditions can vary, depending on the particular application and motor design. Montesano *et al.* [4] employed a finite-element approach towards the structural modeling of the given motor configuration. In the present study, a cylindrical-grain configuration allows for a simpler approach via thick-wall theory, as reported in [5,6]. The radial deformation dynamics of the propellant/casing are modeled by a series of independent ring elements along the length of the motor. Reference structural properties are assumed for an ammonium-perchlorate/hydroxyl-terminated polybutadiene (AP/HTPB) composite propellant surrounded by an aluminum casing.

The quasi-steady burning rate may be ascertained as a function of various parameters, such as a function of local static pressure p , core flow velocity u (erosive burning component), and normal/lateral/longitudinal acceleration, such that:

$$r_{b,qs} = r_p + r_u + r_a \quad (7)$$

The pressure-based burning component may be found through de St. Robert's law [1]:

$$r_p = Cp^n \quad (8)$$

More elaborate equations for the dependency of burning rate on pressure may be utilized, if the de St. Robert representation is not suitable. In the case where the burning rate coefficients are not accurately known, one can undertake a number of simulation runs using a range of guessed values, to iteratively narrow down what the coefficient values are likely to be, in comparing to pressure-time firing data.

The flow-based erosive burning component (negative and positive; see [7]) is established through the following expression [8]:

$$r_b = \frac{r_b}{r_o} \Big|_{\delta_r} \cdot r_o + r_e \quad (9)$$

where at lower flow speeds, the negative component resulting from a stretched combustion zone thickness ($\delta_r > \delta_o$) may cause an appreciable drop in the base burn rate r_o . The stretching of the flame zone at low speed may be viewed as being the result of a laminar-like sliding process of the local axial flow in the boundary layer acting to extend and curve the path of a representative particle moving up from the burning surface towards the flame front, such that the effective reactive length is increased. From [8], in the low-speed regime, the following expression may be applied, such that the core flow Darcy-Weisbach friction factor f is below the limit value f_{lim} at which point negative erosive burning is no longer in effect:

$$\frac{r_b}{r_o} \Big|_{\delta_r} = \cos[\tan^{-1}(K_\delta \delta_o [1 - (f / f_{lim})^{1/2}] \frac{\rho u_\infty}{\rho_s r_o})], f < f_{lim} \tag{10}$$

The parameter K_δ is a shear layer coefficient, whose value set at 2600 m^{-1} , along with a value for f_{lim} of 2.5×10^{-4} , produced a good comparison to experimental data for various solid propellants (composite and double-base) and motors (see Figure 2 for one classical example profile showing the characteristic “dipping” effect on r_b/r_o observed with negative erosive burning, at low axial flow speed; [8,9]). At higher flow speeds, the positive erosive burning component r_e , established from a convective heat feedback premise [8], should dominate:

$$r_e = \frac{h(T_f - T_s)}{\rho_s [C_s(T_s - T_i) - \Delta H_s]} \tag{11}$$

One can find the effective convective heat transfer coefficient h as a function of the zero-transpiration (zero blowing) value h^* and overall burning rate r_b [8,10]:

$$h = \frac{\rho_s r_b C_p}{\exp(\frac{\rho_s r_b C_p}{h^*}) - 1} \tag{12}$$

In turn, the value for h^* may be found as a function of the zero-transpiration Darcy-Weisbach friction factor f^* , via Reyonolds analogy [8]:

$$h^* = \frac{C_p \rho u_\infty (f^*)}{Pr^{2/3} 8} \tag{13}$$

In the realm of fully-developed turbulent flow, Colebrook’s [11] semi-empirical expression for f^* has proven accurate over a wide range of Reynolds numbers:

$$(f^*)^{-1/2} = -2 \log_{10} \left[\frac{2.51}{Re_d (f^*)^{1/2}} + \frac{\varepsilon / d}{3.7} \right] \tag{14}$$

Through Equation 14, one can see the correlation of propellant surface roughness height ε and grain port diameter d_p in influencing the magnitude of flow-dependent erosive burning. For the above case, where the base burning rate r_o is a function of the other mechanisms (pressure and acceleration), one finds the velocity-based component of burn rate from Equation 9 via $r_u = r_b - r_o$. At higher flow speeds, r_u becomes equivalent to r_e .

The effect of normal acceleration a_n resulting from spinning the motor may be determined via [12]:

$$r_b = \left[\frac{C_p (T_f - T_s)}{C_s (T_s - T_i) - \Delta H_s} \right] \frac{(r_b + G_a / \rho_s)}{\exp[C_p \delta_o (\rho_s r_b + G_a) / k] - 1} \tag{15}$$

where the compressive effect of normal acceleration and the dissipative effect of steady longitudinal (or lateral, if say for a star grain configuration) acceleration a_ℓ is stipulated through the accelerative mass flux G_a :

$$G_a = \left\{ \frac{a_n P}{r_b} \frac{\delta_o}{RT_f} \frac{r_o}{r_b} \right\}_{\phi=0^\circ} \cos^2 \phi_d \tag{16}$$

Note that the longitudinal/lateral-acceleration-based displacement orientation angle ϕ_d is greater than the nominal acceleration vector orientation angle (ϕ ; zero when only normal acceleration a_n relative to the burning propellant surface is present; [12]):

$$\phi = \tan^{-1}\left(\frac{a_\ell}{a_n}\right) \tag{17}$$

and:

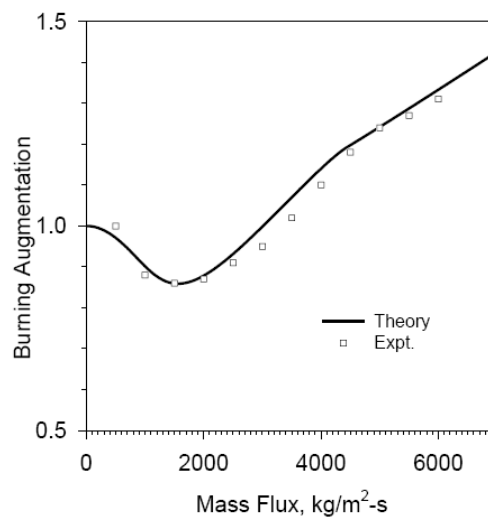
$$\phi_d = \tan^{-1}\left[K\left(\frac{r_o}{r_b}\right)^3 \tan \phi\right] \tag{18}$$

One should also note that a_n is negative when acting to compress the combustion zone, and treated as zero when directed away from the zone. The value for K in Equation 18 has been found to be around 8, when comparing to available experimental data [12,13]. The base ideal combustion zone thickness δ_o is determined as a function of the base burning rate r_o via [12]:

$$\delta_o = \frac{k}{\rho_s r_o C_p} \cdot \ln\left[1 + \frac{C_p(T_F - T_S)}{C_s(T_S - T_i) - \Delta H_s}\right] \tag{19}$$

For the above case, where the base burning rate r_o is a function of the other flow mechanisms (pressure and core flow), one finds the acceleration-based component of burn rate from Equation 15 via $r_a = r_b - r_o$. Note, for the sake of brevity, that the example numerical results presented in this paper will be restricted to pressure- and flow-dependent burning situations.

Figure 2. Theoretical and experimental [8,9] data for burning rate augmentation as a function of mass flux (ρu_∞), double-base solid propellant.



3. Results and Discussion

The characteristics of the baseline reference motor for this simulation study are listed in Table 1. In the case where the given propellant characteristic was not directly measurable or available, such as mean propellant burning surface temperature T_S , assigned values are estimates, for the most part taken from the open or confidential literature, for comparable propellants. The motor is employing an

AP/HTPB composite propellant. The motor is a smaller cylindrical-grain design with an aluminum casing, with a relatively large length-to-diameter ratio. As noted earlier, for brevity, the focus of the present study will be on cases involving single-phase flow (gas only; no substantial inert or reactive particle loading incorporated in the simulation runs) and non-spinning motors.

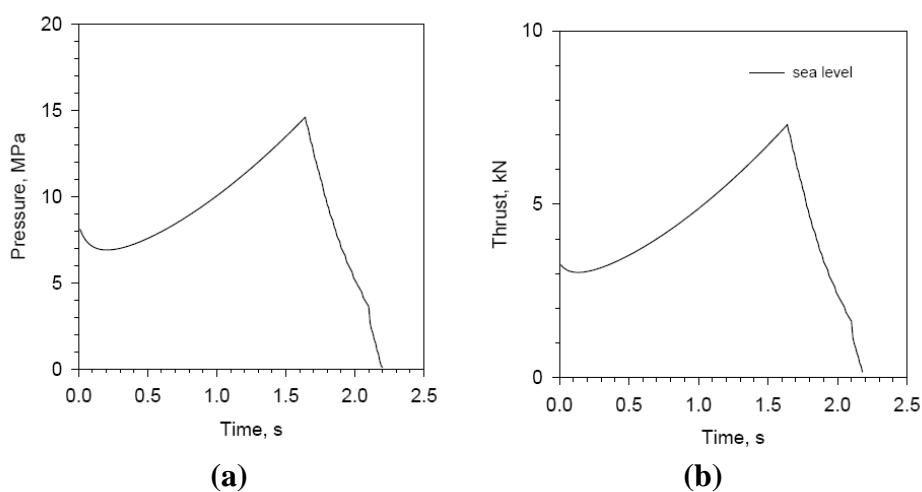
Table 1. Reference motor characteristics.

| Characteristic | Value |
|--|---|
| Propellant grain length, ℓ_p | 84 cm |
| Initial port diameter, $d_{p,i}$ | 2.1 cm |
| Final port diameter, $d_{p,f}$ | 6.35 cm |
| Nozzle throat diameter, d_t | 2.03 cm |
| Nozzle exit diameter, d_e | 7.0 cm |
| Grain/nozzle-convergence length ratio, ℓ_p/ℓ_c | 16:1 |
| Propellant specific heat, C_s | 1500 J/kg-K |
| Propellant density, ρ_s | 1740 kg/m ³ |
| Propellant thermal conductivity, k_s | 0.4 W/m-K |
| Propellant thermal diffusivity, α_s | 1.54×10^{-7} m ² /s |
| Propellant flame temperature, T_f | 3060 K |
| Propellant surface temperature, T_s | 1130 K |
| Propellant initial temperature, T_i | 294 K |
| Gas specific heat, C_p | 1845 J/kg-K |
| Specific gas constant, R | 320 J/kg-K |
| Gas thermal conductivity, k | 0.2 W/m-K |
| Gas absolute viscosity, μ | 8.8×10^{-5} kg/m-s |
| Gas specific heat ratio, γ | 1.21 |
| De St. Robert exponent, n | 0.33 |
| De St. Robert coefficient, C | 0.05 cm/s-(kPa) ⁿ |
| Particle mass fraction, α_p | 0% |
| Propellant elastic modulus, E_A | 45 MPa |
| Propellant Poisson's ratio, ν_A | 0.497 |
| Casing inner wall radius, r_m | 3.24 cm |
| Casing wall thickness, h_B | 0.127 cm |
| Casing material density, ρ_B | 2700 kg/m ³ |
| Casing elastic modulus, E_B | 80 GPa |
| Casing material Poisson's ratio, ν_B | 0.33 |

Example chamber (head-end) pressure-time and sea-level thrust-time profiles, for the reference motor, are provided in Figure 3. Assuming a reasonably effective nozzle design for a quasi-one-dimensional thrust estimate [14], for a nominal nozzle exit-to-throat area expansion of 11.9, the delivered average specific impulse for the sea-level firing is around 240 s. In Figure 3a, one can observe the early influence of erosive burning in causing the pressure to be higher in the initial stages of the simulated quasi-steady firing (a little over 1 MPa above what would have been the base pressure-dependent-burning curve, initially at $t = 0$ s, subsequently subsiding for the most part by $t = 0.2$ s). The erosive burning is strengthened by the lower port diameter that is present at this early juncture. In an actual experimental test firing of a comparable motor, one may observe an even more pronounced

ignition peak or spike [2,15] with the additional energy input of the motor's igniter complementing that of the motor's solid propellant. Conversely, if the ignition process is a more drawn-out process, with a progressive left-to-right (upstream-to-downstream) ignition of the solid propellant (rather than a more uniform, more rapidly distributed ignition), one may see an early head-end pressure curve that lies below the quasi-steady estimate for that instant in the firing. An early transient dilation (outward deflection) of a portion of the propellant grain as it undergoes a distributed ignition might also effectively reduce the erosive burning influence on the head-end pressure curve early on [2]. Given these factors, it is not unusual to find that quasi-steady profiles that have neglected erosive burning can, on occasion, compare better to the actual experimental profile than when the influence of erosive burning was included in the simulation. It is important to keep these transient factors in mind, and to realize that the ignition transient phase can have a lingering effect on the follow-on shape of the pressure-time profile (and the corresponding thrust-time profile), substantially beyond the ignition transient itself. Since a quasi-steady firing profile (usually) assumes an instantaneous ignition/fill process (rather than a distributed process over a finite period of time, say 50 to 100 ms for the reference motor of this study), and propagates in time from that assumption, one has to anticipate some differences will exist between that simulated profile and the corresponding experimental profile.

Figure 3. (a) Predicted head-end pressure profile for small cylindrical-grain SRM; (b) Corresponding predicted thrust profile.



Moving to the graphs in Figure 4, one sees a comparison between the effects of including or neglecting negative erosive burning on the simulated pressure-time profile at the reference propellant surface roughness of $400\ \mu\text{m}$ (only a minor difference apparent between the two, visible later in the firing), and the corresponding grain port profiles. Both port profiles reflect the appearance of substantial positive erosive burning aft in the early portions of the firing. Later in the firing, one sees the telltale trough in the dashed grain profile curves near the head end, a phenomenon that one associates with appreciable negative erosive burning. The deepest trough point in each of the dashed curves appears to move rightward with time into the firing, in correlation with an increasing port diameter. Note that the roughness height value of $400\ \mu\text{m}$ comes from the nominal peak AP crystal diameter used by some comparable composite-propellant experimental motors in the literature [2].

Figure 4. (a) Predicted head-end pressure profile for reference cylindrical-grain SRM, with and without a negative erosive burning model component, at reference propellant surface roughness; (b) Predicted port grain radius profile from head-end (left) to port exit (right), with (dashed curves) and without a negative erosive burning model component (solid curves), at 0.25-sec increments (curves move upward as the grain burns back, from the initial port radius of 1.05 cm, towards the upper insulation/wall boundary at a radius of 3.175 cm).

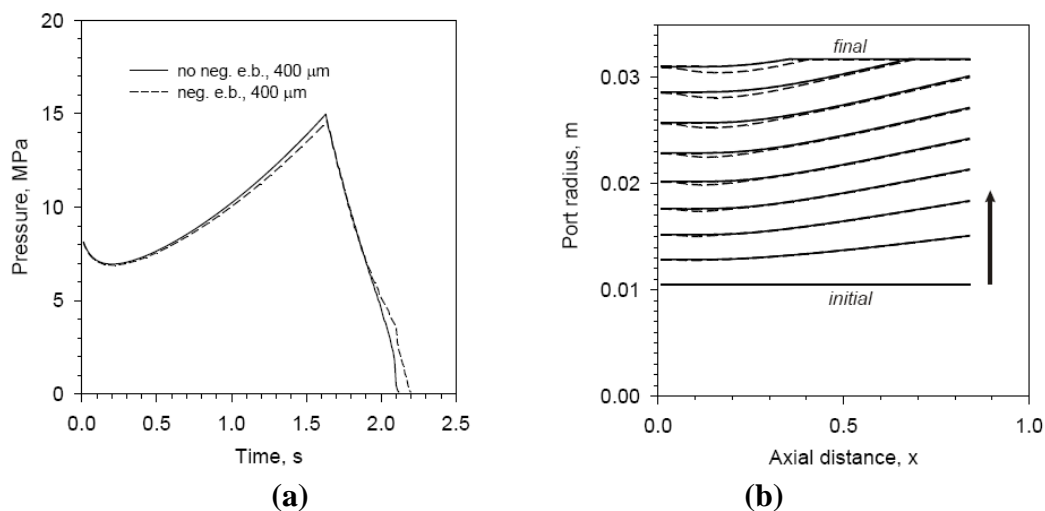


Figure 5 illustrates the corresponding results for a relatively smooth 10- μm propellant surface roughness. Since positive erosive burning is strongly dependent on propellant surface roughness, one can see that the initial peak in the pressure profiles of Figure 5a is almost absent, versus Figures 3 or Figure 4. There is clearly a wider difference in the two pressure-time curves of Figure 5a, with negative erosive burning being stronger at 10 μm roughness, pulling down the pressure-time profile and thus extending the time of the firing. The starting deepest trough point for the negative-erosive-burning grain profile of Figure 5b is further right, versus the 400- μm case. Similar to Figure 4b, the deepest trough point progresses further right with time into the firing, indicating a function of increasing port diameter.

The effects of propellant and casing dynamic deflection have been considered in past combustion instability studies (see [4,6]). Here, we are interested in looking at quasi-steady outward deflection of the propellant and surrounding casing under pressure loading, and how this affects the resulting internal ballistics of the motor. Allowing for this deflection, one can compare the rigid to the nonrigid case, for the corresponding pressure-time profiles, as illustrated in Figure 6a for the reference motor of Figure 3. The nonrigid pressure curve is slightly lower early in the firing, and slightly higher later in the firing. Observing the corresponding curves for an unloaded grain (dashed) versus a pressure-loaded (solid curves) grain in Figure 6b, the outward deflection of the propellant grain is evident, but small. A larger port diameter early reduces positive erosive burning, and later, increases the burning surface area for the predominant pressure-dependent burning, as reflected by the corresponding pressure-time profiles. It is commonplace for quasi-steady internal ballistic simulation models in use today to assume the propellant is rigid over the course of firing. The internal ballistic results for the example motor of Figure 6 suggest that the differences arising from a rigid versus non-rigid assumption can in fact be quite small.

Figure 5. (a) Predicted head-end pressure profile for reference cylindrical-grain SRM, with and without a negative erosive burning model component, at a low propellant surface roughness of $10\mu\text{m}$; (b) Predicted port grain radius profile, with (dashed curves) and without a negative erosive burning model component (solid curves), at 0.25-sec increments.

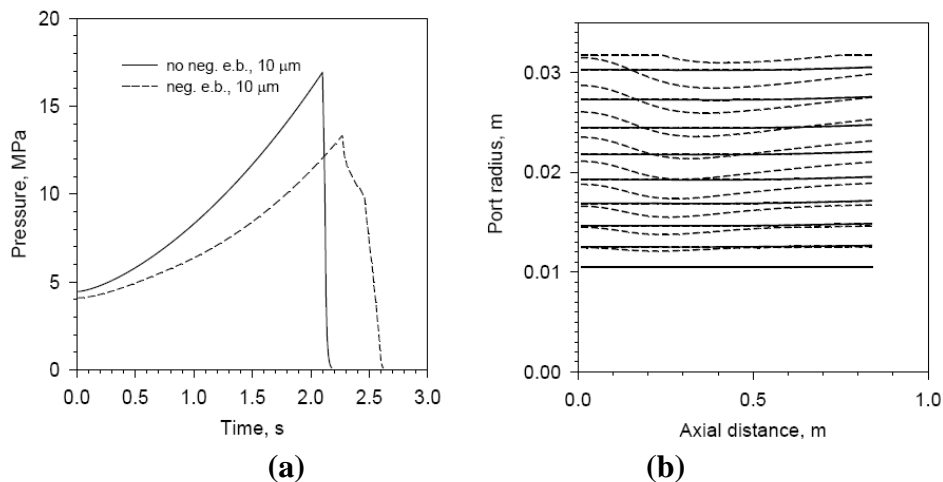
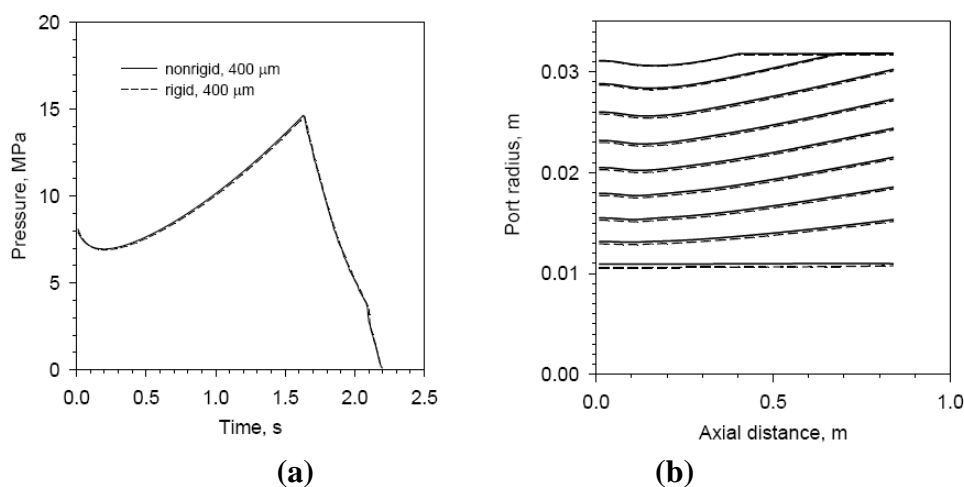


Figure 6. (a) Predicted head-end pressure profile for small cylindrical-grain SRM, rigid and nonrigid cases; (b) Predicted port grain radius profile, with (solid curves) and without pressure loading (dashed curves), at 0.25-sec increments.



The effects of scaling up a motor to larger and larger sizes can now be looked at. For example, consider the results presented in Figure 7 for inclusion and absence of negative erosive burning, for a motor which has been scaled up by eight times (grain length, initial and final port diameter, nozzle throat diameter, nozzle exit diameter). In comparing to the original motor of Figure 4, one can see a wider difference between the two pressure-time curves, which suggests a correlation to stronger negative erosive burning with higher port diameters, as observed earlier. There is only a very small initial peaking evident in the Figure 7a p_c - t profiles before subsiding quickly to the base pressure-dependent-burning curve, with the weakened positive erosive burning component. Referring to Figure 7b, the negative-erosive-burning grain profiles display a much deeper trough relative to that seen in Figure 4b, and the deepest point is shifted further to the right. The thrust-time profile for the negative erosive burning run is provided by Figure 8, as a comparison to Figure 3b in scaling up eight

times (one can note the correlation to the square of the length increase, in producing a thrust about 64 times greater, later into the firing). The average sea-level specific impulse was slightly lower than the smaller motor's value mentioned earlier.

Figure 7. (a) Predicted head-end pressure profile for cylindrical-grain SRM eight times bigger in size than reference motor (see Figure 4a), with and without a negative erosive burning model component, at reference propellant surface roughness; (b) Predicted port grain radius profile from head-end (left) to port exit (right) for 8× scaled-up SRM (see Figure 4b to compare to baseline), with (dashed curves) and without a negative erosive burning model component (solid curves), at 2.0-sec increments.

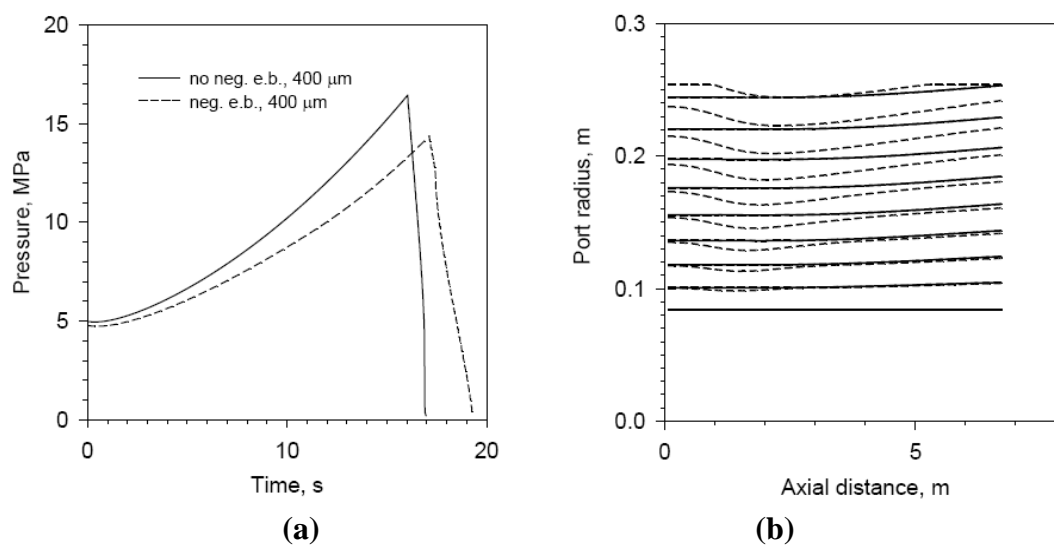
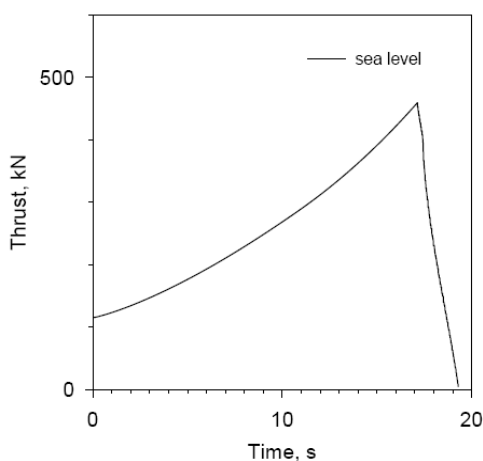


Figure 8. Predicted thrust profile for scaled-up cylindrical-grain SRM.



One can compare the rigid to the nonrigid case, for the corresponding pressure-time profiles, as illustrated in Figure 9a for the scaled-up motor of Figure 7. The nonrigid pressure curve aligns with the rigid curve early in the firing, and becomes slightly higher later in the firing. Observing the corresponding curves for an unloaded grain (dashed) versus a pressure-loaded (solid curves) grain in Figure 9b, the outward deflection of the propellant grain is evident, but quite small (in relative terms, smaller than that seen in Figure 6b for the smaller reference motor). A larger port diameter early

nominally reduces positive erosive burning, and later, increases the burning surface area for the predominant pressure-dependent burning, as reflected by the corresponding pressure-time profiles.

Figure 9. (a) Predicted head-end pressure profile for 8× scaled-up cylindrical-grain SRM, rigid and nonrigid cases; (b) Predicted port grain radius profile for 8× scaled-up cylindrical-grain SRM, with (solid curves) and without pressure loading (dashed curves), at 2.0-sec increments.

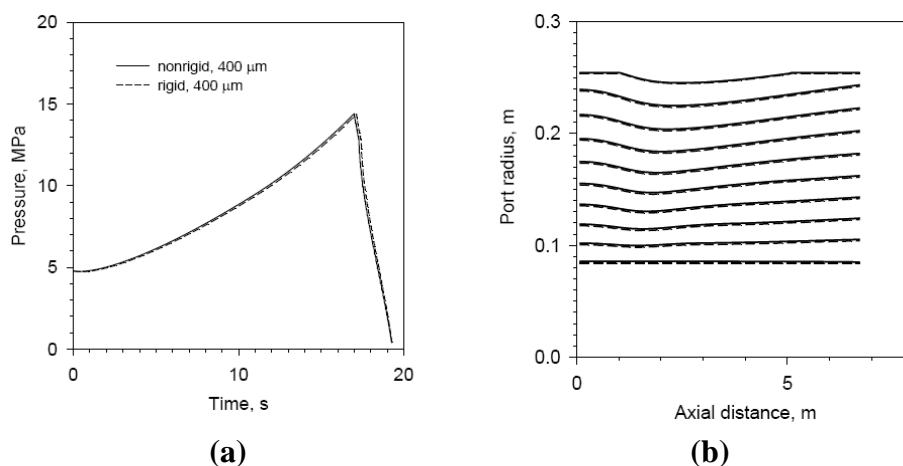
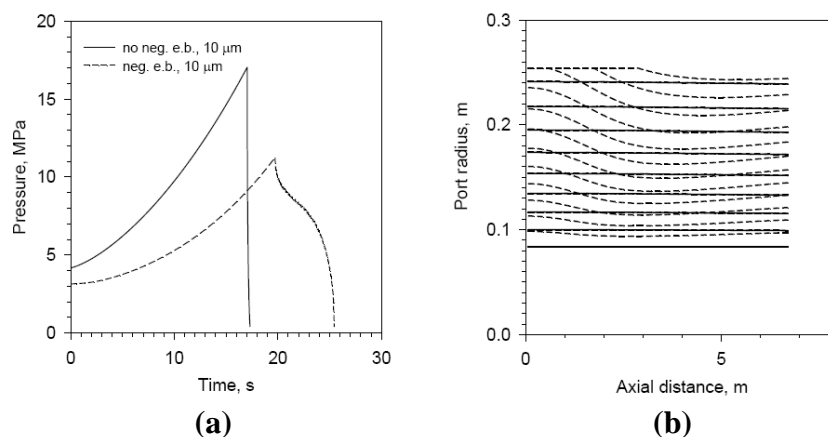


Figure 10 illustrates the results for a 10- μm propellant surface roughness (rigid case, with and without inclusion of the negative erosive burning component). Since positive erosive burning is strongly dependent on propellant surface roughness as well as port diameter, one can see that the initial spike in the pressure profiles of Figure 10a are effectively absent, as compared to Figure 7a at a 400- μm roughness.

Figure 10. (a) Predicted head-end pressure profile for cylindrical-grain SRM eight times bigger in size than reference motor (see Figure 5a), with and without a negative erosive burning model component, at a 10- μm propellant surface roughness. (b) Predicted port grain radius profile from head-end (left) to port exit (right) for 8× scaled-up SRM (see Figure 5b to compare to baseline), with (dashed curves) and without a negative erosive burning model component (solid curves), at 2.0-sec increments.



There is clearly a wider difference in the two pressure-time curves of Figure 10a as compared to 7a, with negative erosive burning being stronger at 10 μ m roughness, pulling down the pressure-time profile and thus extending the time of the firing. The starting deepest trough point for the negative-erosive-burning grain profile of Figure 10b is further right (and gets relatively deeper with time), versus the 400- μ m case of 7b. Similar to Figure 7b, the deepest trough point progresses further right with time into the firing, indicating a function of increasing port diameter.

4. Conclusions

The predicted effect of negative/positive erosive burning on the quasi-steady firing profile of a cylindrical-grain motor, as influenced by propellant surface roughness and port diameter, has been made evident by the numerical results presented in this paper. While it is well known that an increasing port diameter and lower propellant surface roughness reduces positive erosive burning, and the present numerical results reflect these observations, it is of interest to note the significant influence that negative erosive burning has on some of the predicted firing profiles, at lower propellant surface roughnesses and larger port diameters especially. With this in mind, one should note that some internal ballistic simulation models in use today do not include any consideration for negative erosive burning. Some existing models do include empirical correction factors to bring predictions closer to the experimental result (e.g., the ballistic anomaly rate factor [BARF] approach [16] to correct for perceived “humping” or “rainbowing” of the experimental p_c - t profile relative to the predicted profile). It remains to be determined whether the two significant parameters that frame the present negative erosive burning model, f_{lim} and K_δ , have in practice some variation in their values, say as a function of port diameter or some propellant characteristic. More negative erosive burning experiments for different solid propellants at different spatial scales (*i.e.*, port diameters) would help clarify that potential issue as part of an experimental validation process. Of course, the larger the motor, the more costly is the experiment. Also, larger production SRM propellant grains are commonly segmented (for ease and quality of propellant casting) rather than fabricated as one continuous block. A left-to-right series of cylindrical segments (commonly referred to as a BATES [ballistic test and evaluation system] configuration [14]), with some separation between each segment, will produce an altered core-flow boundary layer profile moving downstream from segment to segment through the motor chamber, as compared to one long continuous channel (port) from the head end to the nozzle entry as per Figure 1.

In terms of the examples presented in this paper, structural deflection of the propellant/casing assembly did not play an overly significant role in altering the predicted quasi-steady firing profile, regardless of motor size. The behaviour expected for a small increase in port cross-sectional area along the propellant grain was essentially as expected. It remains to be seen whether structural deflection magnitudes in a transient situation, say during the ignition phase, might be of more significance, in some cases, in influencing the resulting predicted pressure-time firing profile. Of course, the propellant's Poisson ratio value (ν_d) will have some bearing on the degree of deflection that might be observed.

References

1. Sutton, G.P.; Biblarz, O. *Rocket Propulsion Elements*, 7th ed.; John Wiley & Sons: New York, NY, USA, 2001; pp. 428–433, 430–453.

2. Greatrix, D.R.; Gottlieb, J.J.; Constantinou, T. Quasi-steady analysis of the internal ballistics of solid-propellant rocket motors. *Can. Aeronaut. Space J.* **1987**, *33*, 61–70.
3. Gottlieb, J.J.; Greatrix, D.R. Numerical study of the effects of longitudinal acceleration on solid rocket motor internal ballistics. *J. Fluids Eng.* **1992**, *114*, 404–410.
4. Montesano, J.; Behdinin, K.; Greatrix, D.R.; Fawaz, Z. Internal chamber modeling of a solid rocket motor: Effects of coupled structural and acoustic oscillations on combustion. *J. Sound Vib.* **2008**, *311*, 20–38.
5. Greatrix, D.R.; Harris, P.G. Structural Vibration Considerations for Solid Rocket Internal Ballistics Modeling. In Proceedings of AIAA/ASME/SAE/ASEE 36th Joint Propulsion Conference, Huntsville, AL, USA, July 2000; AIAA Paper No. 2000-3804.
6. Baczynski, C.; Greatrix, D.R. Grain Geometry Modifications for Instability Symptom Suppression in Solid Rocket Motor. In Proceedings of AIAA/ASME/SAE/ASEE 44th Joint Propulsion Conference, Hartford, CT, USA, July 2008; AIAA Paper No. 2008-4600.
7. Razdan, M.K.; Kuo, K.K. Erosive Burning of solid propellants. In *Fundamentals of Solid Propellant Combustion*, Kuo, K.K., Summerfield, M., Eds.; AIAA Publications: Washington, DC, USA, 1984; Volume 90; Chapter 10; pp. 515–598.
8. Greatrix, D.R. Model for prediction of negative and positive erosive burning. *Can. Aeronaut. Space J.* **2007**, *53*, 13–21.
9. Godon, J.C.; Duterque, J.; Lengellé, G. Solid Propellant Erosive Burning. In Proceedings of AIAA/ASME/SAE/ASEE 23rd Joint Propulsion Conference, San Diego, CA, USA, July 1987; AIAA Paper No. 87-2031.
10. Mickley, H.S.; Ross, R.C.; Squyers, A.L.; Stewart, W.F. *Heat, Mass, and Momentum Transfer for Flow over a Flat Plate with Blowing or Suction*. Technical report for Massachusetts Institute of Technology: Cambridge, MA, USA, July 1954. NACA Report TN3208
11. Streeter, V.L. *Fluid Mechanics*, 3rd ed.; McGraw-Hill: New York, NY, USA, 1962; pp. 213–222.
12. Greatrix, D.R. Parametric analysis of combined acceleration effects on solid-propellant combustion. *Can. Aeronaut. Space J.* **1994**, *40*, 68–73.
13. Greatrix, D.R. Internal Ballistic Model for Spinning Star-Grain Motors. *J. Propul. Power* **1996**, *12*, 612–614.
14. Greatrix, D.R.; Karpynczyk, J. Rocket vehicle design for small-payload delivery to orbit. *Can. Aeronaut. Space J.* **2005**, *51*, 123–131.
15. Greatrix, D.R.; Gottlieb, J.J.; Constantinou, T. Numerical model for pellet-dispersion igniter systems. *J. Propul. Power* **1988**, *4*, 412–420.
16. McMillin, J.E.; Furfaro, J.A. A Review of ETM-03 (A Five Segment Shuttle RSRM Configuration) Ballistic Performance. In Proceedings of AIAA/ASME/SAE/ASEE 40th Joint Propulsion Conference, Fort Lauderdale, FL, USA, July 2004; AIAA Paper No. 2004-3895.